THE AUTOMATIC PREDICTABILITY OF SUPER GEOMAGNETIC STORMS FROM HALO CMES ASSOCIATED WITH LARGE SOLAR FLARES

HUI SONG, VASYL YURCHYSHYN, GUO YANG, CHANGYI TAN,
WEIZHONG CHEN and HAIMIN WANG
*Center for Solar-Terrestrial Research, New Jersey Institute of Technology, Newark, NJ 07102,
U.S.A.; Big Bear Solar Observatory, 40386 North Shore Lane, Big Bear City, CA 92314, U.S.A.
(e-mail: hxs6800@njit.edu)*

Abstract. We investigate the relationship between magnetic structures of coronal mass ejection (CME) source regions and geomagnetic storms, in particular, the super storms when the D_{st} index decreases below -200 nT. By examining all full halo CMEs that erupted between 1996 and 2004, we selected 73 events associated with M-class and X-class solar flares, which have a clearly identifiable source region. By analyzing daily full-disk MDI magnetograms, we found that the horizontal gradient of the line-of-sight magnetic field is a viable parameter to identify a flaring magnetic neutral line and thus can be used to predict the possible source region of CMEs. The accuracy of this prediction is about 75%, especially for those associated with X-class flares (up to 89%). The mean orientation of the magnetic structures of source regions was derived and characterized by the orientation angle θ, which is defined to be $\leq 90°$ in the case of the southward orientation and $\geq 90°$, when the magnetic structure is northwardly oriented. The orientation angle was calculated as the median orientation angle of extrapolated field lines relative to the flaring neutral line. We report that for about 92% of super storms (12 out of 13 events) the orientation angle was found to be southward. In the case of intense and moderate storms ($D_{st} \geq -200$ nT), the relationship is less pronounced (70%, 21 out of 30 events). Our findings demonstrate that the approach presented in this paper can be used to perform an automatic prediction of the occurrence of large X-class flares and super geomagnetic storms.

1. Introduction

One of the main objectives in space weather research is to predict the occurrence of geomagnetic storms based on real-time solar observations. A severe geomagnetic storm may produce many harmful effects on the Earth, such as radiation hazards to humans, especially to astronauts, disruption of communication, navigation and satellite control systems, damage of electric power grids, and so on. A geomagnetic storm is initiated when the energy is transferred from the Sun to the Earth's magnetosphere through a coronal mass ejection (CME) that is launched at the Sun. Usually, the Earth's magnetosphere is a closed structure and no energy and particles can be injected into it. Therefore, a geomagnetic storm can only occur when the interplanetary magnetic field (IMF) turns southward and remains so for some period of time (e.g., Bothmer and Schwenn, 1995; Tsurutani *et al.*, 1998; Tsurutani, 2001).

Reconnection between southward IMF and the northwardly directed geomagnetic field occurs at the day side magnetopause and this reconnection transports energy from the solar wind into the magnetosphere (Dungey, 1961). This reconnection stresses the Earth's magnetic field and the degree of the stress, the Disturbance Storm Time (D_{st}) Index, is a measure of the intensity of a geomagnetic storm. It is expressed in nanoTesla and is based on the average value of the horizontal component of the Earth's magnetic field measured hourly at four near-equatorial geomagnetic observatories. Large negative values of D_{st} indicate a strong geomagnetic storm. A geomagnetic storm has three distinct phases of evolution: (1) initial phase, lasting from minutes to hours, when D_{st} increases up to tens of nanoTesla; (2) main phase, lasting from 0.5 h to several hours during which D_{st} drops below zero, down to minus hundreds of nanoTesla; (3) recovery phase lasting tens of hours to days, when the D_{st} index gradually returns to the normal (undisturbed) level. Currently, the Advanced Composition Explorer (ACE) spacecraft, which orbits the L1 Lagrangian point of Earth–Sun gravitational equilibrium located about 1.5 million km from the Earth, performs measurements of the direction and magnitude of IMF. This excellent position enables ACE to conduct 24 h monitoring of solar wind condition and to transmit interplanetary data in real time that can provide 1 h advance warning of geomagnetic storms.

The following storm classification has been proposed by Gonzalez *et al.* (1994): (1) small storm, D_{st} is in the range between -30 and -50 nT; (2) moderate storms, D_{st} between -50 and -100 nT; (3) strong storms, D_{st} is -100 nT or stronger. Another parameter that describes the intensity of geomagnetic storm is K-index. It has a range from 0 to 9 and is directly related to the maximum amount of fluctuation (relative to a quiet day) in the geomagnetic field over a 3-h interval. Due to the difference in location of geomagnetic observatories, the officially index that is used is K_p, which is derived by calculating a weighted average of K-indices from a network of geomagnetic observatories.

Severe geomagnetic storms are mainly related to powerful CMEs that are expelled from the solar atmosphere. Now it is well accepted that the front-side halo CMEs are the major causes for such storms (e.g., Brueckner *et al.*, 1998; Cane, Richardson, and St. Cyr, 2000; Gopalswamy *et al.*, 2000; Webb *et al.*, 2000; Wang *et al.*, 2002; Zhang *et al.*, 2003). A halo CME, first introduced by Howard *et al.* (1982), is described as a shell-like CME heading either toward the Earth if it arises on the front-side of the Sun, or away from the Earth if it is on the backside. Cane, Richardson, and St. Cyr (2000) showed that only about half of front-side halo CMEs encounter the Earth and their associated solar events typically occur at longitudes ranging from 40° East to 40° West. According to Wang *et al.* (2002), about 45% of total 132 Earth-directed halo CMEs caused geomagnetic storms with $K_p \leq 5$, and almost 83% of events took place within $\pm 30°$ of the central meridian of the Sun. Similar study on the *interplanetary CMEs* (ICMEs) estimated that their geoeffectiveness ranges from 25% (Vennerstroem, 2001) up to 82% (Wu and Lepping, 2002). Park *et al.* (2002) reported that the geoeffectiveness of flares

is about 30–45%. Howard and Tappin (2005) performed a statistical analysis of CME/ICMEs events from January 1998 to August 2004 and concluded that only around 40% of the shock/storms at 1 AU were associated either with an X-class or M-class flares.

Previous studies had shown that filament chirality and the orientation of filament magnetic fields correspond to the chirality and orientation of the magnetic field in the associated magnetic clouds (MCs) (Bothmer and Schwenn, 1994; Rust, 1994; Marubashi, 1997; Yurchyshyn *et al.*, 2001; Yurchyshyn, Hu, and Abramenko, 2005). A magnetic cloud is an interplanetary structure with strong magnetic fields, low proton temperatures and a smooth rotation of the magnetic field direction through a large angle as it moves past a spacecraft in a period on the order of a day (Burlaga *et al.*, 1981). These results suggest that immediately after the eruption one may be able to predict the orientation of the MC associated with the CME and, furthermore, the likelihood of a geomagnetic storm.

In order to advance our current understanding of the relationship between CMEs and geomagnetic storms, we need a deeper knowledge of solar magnetic field that is the main source of energy for solar eruptions. Because of lack of direct measurements of the coronal magnetic field, extrapolation of the photospheric measurements upward into the corona is the primary means to reconstruct coronal magnetic structure and analyze magnetic connectivity. There are variety of extrapolation techniques such as potential, force-free and nonforce-free field methods. For an automated, real-time magnetic field simulations, we choose a potential field model, which requires least human intervention, a minimum set of initial assumptions and boundary conditions and thus enables us to analyze magnetic configuration of the CME source regions in the real time.

The objective of this work is to better understand the relationship between surface magnetic structures and the geomagnetic index (B_z or D_{st}). In this paper, observations are described in Section 2, data analysis in Section 3. Statistical results are listed in Section 4. Finally, we present conclusions and discussions in Section 5.

2. Data Sets

Beginning from middle 1990s more advanced data on CMEs and IMF became available from space observatories such as SOHO, ACE, and WIND. They provide unprecedented opportunity to study and forecast space weather. In this study, we use the following data:

(1) Data from LASCO coronagraphs C2 and C3 that image Thomson-scattered visible light taken through a broadband filter onboard SOHO. The data allow us to determine the occurrence of CMEs and their speeds. The CME Catalog, generated and maintained at the CDAW data center and NASA, covers the period from 1996 to present (Yashiro *et al.*, 2004). For each event

it provides, among others, height–time plots, plane-of-sky speeds, and CME onset time recorded by their first appearance in LASCO/C2, position angle, corresponding accelerations and so on. The CME speeds are determined from both linear and quadratic fits to the height–time measurements. In our study, we used the linear (constant speed) fit. This choice is based on the study by MacQueen and Fisher (1983) who showed that flare associated CMEs tend to display little or no acceleration beyond the edge of the occulting disk (1.2 $R_\odot$).

(2) Intensities of geomagnetic storms, measured by hourly equatorial D_{st} values from the World Data Center for Geomagnetism in Kyoto.[1] Since the storms with $D_{st} \leq -200$ nT are the most disastrous phenomena in space weather, for the purpose of this study we regrouped geomagnetic storms as follows: moderate storms are in the range of -30 to -100 nT, intense storms are between -100 and -200 nT and super storms are those with the D_{st} index less than -200 nT.

(3) Solar activity reports that are available online from the NOAA Space Environment Center.[2] Solar flare reports include the Coordinated Universal Time (UTC) of the beginning, maximum and end of a flare, the X-ray flux at the flare peak and the location of the flare, if available. In our study, we associated solar flares with the corresponding halo CMEs by matching their onset times.

(4) Magnetic Field Experiment (MAG) onboard ACE satellite provides 1-h averages of magnetometer data, which are used to study structure of IMF. MAG measurements, in particular, the southward component, B_z, are used to forecast intensity of geomagnetic storms.

(5) SOHO's Michelson Doppler Imager (MDI) provides full-disk line-of-sight magnetograms at the photospheric layer with a spatial resolution of 4′. These magnetograms were used to analyze the structure of magnetic fields in CME source regions.

3. Methods of Data Analysis

Halo CMEs are classified according to their angular width into either partial or full halo CMEs. Here we concentrate only on full halo CMEs, which are defined as those having 360° span angle as indicated in the LASCO CME Catalog. Based on this criteria, we selected 318 full halo CMEs that occurred during 1996–2004. The identification of the geomagnetic storms, associated with these CMEs, was composed of two steps: (1) identification of the active regions with high probability of CMEs/flares occurrence that is based on full-disk MDI magnetogram; and (2)

[1] http://swdcdb.kugi.kyoto-u.ac.jp/dstdir/.
[2] http://www.sec.noaa.gov/ftpmenu/indices.html.

estimation of the range of intensity of geomagnetic storms based on the observed CME data.

3.1. Identification of possible CME source regions from high gradient neutral lines

There are variety of ways to identify the solar source of a front-side halo CME, such as EIT dimming (Sheeley *et al.*, 1983; Sterling and Hudson, 1997; Webb *et al.*, 2000; Wang *et al.*, 2002), EIT and Moreton waves (Thompson *et al.*, 1999; Warmuth *et al.*, 2004), post-flare loops (Hudson *et al.*, 1998). All these methods, however, are based on the analysis of post-event data. In this paper, we propose a gradient neutral line method that will enable us to identify possible sources of CMEs/flares from solar data taken before the eruptive event.

Eruption of CME is accompanied by release of large amount of energy in a short period of time. In order to store this energy, the magnetic field of the CME source region must be in a stressed, distorted configuration as compared to the minimum-energy potential field configuration. One signature of such a non-potential configuration is strong magnetic shear seen along the active region main neutral line (NL) that divides two opposite polarity magnetic regions. The extent to which the magnetic field is sheared along the main neutral line is a measure of global non-potentiality of an active region (Falconer, 2001; Zhang, 2001). Magnetic shear can be quantitatively described by the angle between the observed and potential transverse fields. Falconer, Moore, and Gary (2003) analyzed 17 vector magnetograms and concluded that when the horizontal gradient of the line-of-sight field ($\nabla B_{\parallel}$, herein, magnetic gradient) is higher than a certain threshold ($50\,\mathrm{G\,Mm}^{-1}$ in their study), the length of a segment of the main NL with strong gradient, L_{SG}, is significantly correlated with CME productivity of an active region. In a study of six large (X5 or larger) flares , Wang *et al.* (2005) reported on the positive linear relationship between the magnetic shear and the magnetic gradient and that the latter seems to be a better tool to determine the probability of the occurrence of flares and CMEs in an active region. In this paper, we further examine this conclusion with more events. If this relationship is proved to be viable, then the magnetic gradient method can be used as the first step in an automatic routine to locate the most probable CME/flare source regions.

First, utilizing a full-disk longitudinal MDI magnetogram obtained on the day of a halo CME, we calculated a full-disk magnetic gradient map and masked it with a neutral line map. We then chose $50\,\mathrm{G\,Mm}^{-1}$ (Falconer, Moore, and Gary, 2003) as the threshold to calculate the length of high gradient neutral line (HGNL) at a point with the largest magnetic gradient in the gradient map, and move along the NL in both directions away from the starting point. According to Hagyard (1990), a sufficient condition for a large flare to occur is that the length of the neutral line should be equal or exceed 8–10 Mm. In our study, we accepted that if the length

of HGNL is longer than $\approx 7\,\mathrm{Mm}$ (approximately $10'$), it indicates that the region under study has a non-potential configuration and the probability of occurrence of CMEs and/or flares is high. Otherwise, we proceed to the next largest gradient point in the map and perform similar analysis again, until all neutral lines are evaluated. Then, using the first qualified gradient point as center, we cropped the full disk MDI magnetogram into a small map (Figure 1) with a field of view of about $300'' \times 200''$. This size can cover a typical large active region. Both images are presented in negative, i.e., darker points indicate stronger magnetic gradient. The dark thick line shown in the lower panel of Figure 1 is a HGNL and it represents the gradient distribution along the NL. The length of HGNL depends on the gradient threshold values. It becomes shorter and only strongest parts are left as we increase the threshold.

The locations identified by this method are shown in Table I, column 2. The total length of all intervals of HGNL in the identified source region is presented in column 8 as L_{neu}. Note that for several events listed in Table I the $50\,\mathrm{G\,Mm^{-1}}$ magnetic gradient threshold was too large and therefore HGNL is zero.

To verify our identified locations, we used NOAA SEC reports on Hα flares, associated with the selected 318 halo CMEs. Please, note that only those halo CMEs that were associated with M-class or X-class flares whose location was accurately indicated in the Solar Activity Reports are listed in Table I. In those cases, when our predicted location significantly differs from that reported by NOAA, the NOAA coordinates are used. These coordinates are marked in Table I with asterisks.

We studied how the selection of the gradient threshold affects the active region identification. We repeated the process of identification by using several different thresholds: 25, 50, 75, and $100\,\mathrm{G\,Mm^{-1}}$. The results are shown in Table II. The "correct" column shows the number of cases when the active region, identified by the magnetic gradient method, is the same as the one reported by NOAA SEC. This table shows that the magnetic gradient method performs better when the gradient threshold increases. Namely, the probability to detect a source of an X-class flare is much higher then that of an M-class flare.

3.2. ORIENTATION OF CMES

In order to evaluate the geoeffectiveness of CMEs, we will examine the structure of magnetic fields in their source regions. We used a potential field model (Abramenko, 1986) to extrapolate the measured photospheric fields up into the corona. The model assumes that electric currents above the photosphere are negligible and the potential field vanishes faster than $1/R$. The model always provides a good approximation to the observed large scale, steady-state coronal loops, although it is inapplicable to the dynamic solar events. Another reason to choose a potential model is because it can be automatically computed by using readily available line-of-sight magnetograms. Besides, the existing force-free field methods need either vector field measurements
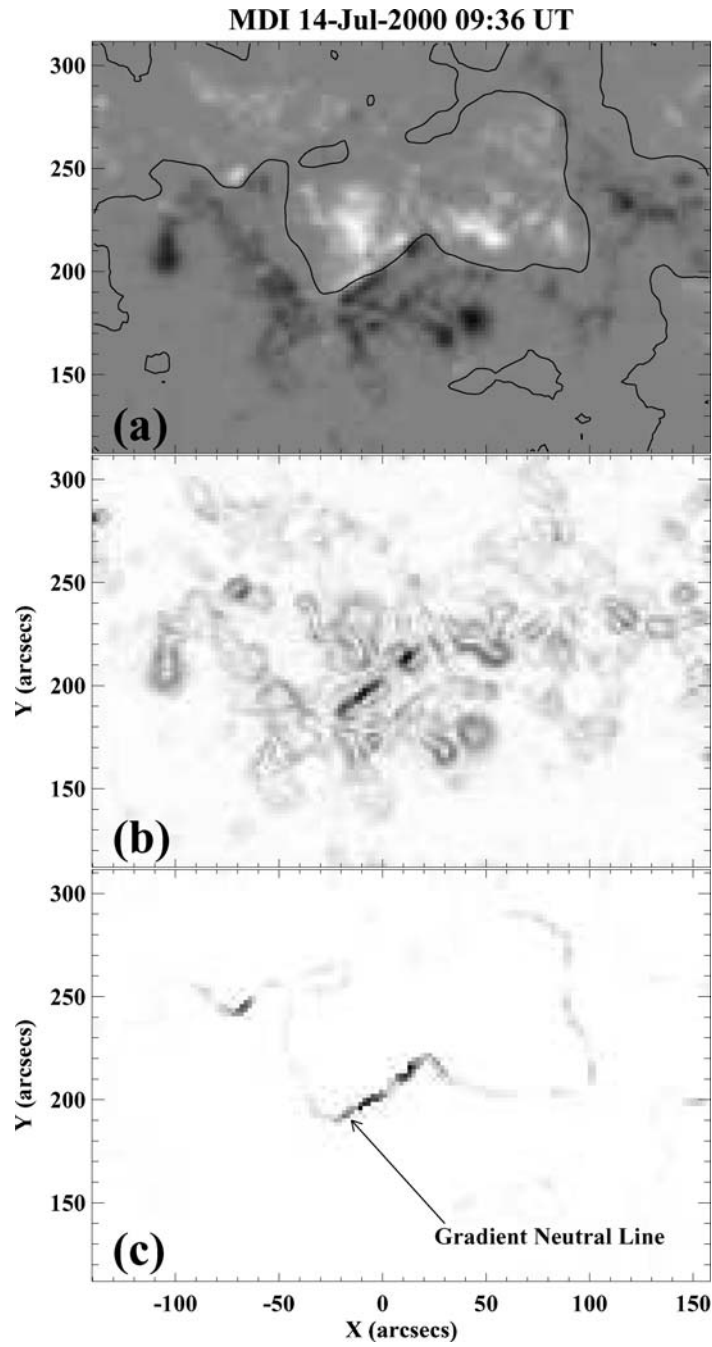
Figure 1. MDI high-resolution magnetogram for AR 9077 taken on July 14, 2000 (*top panel*). *Black contours* are magnetic neutral lines. The *middle panel* (b) shows the corresponding magnetic gradient map. The *bottom panel* (c) is the gradient distribution along the neutral line. *Dark line* is a gradient neutral line.

TABLE I
List of Halo CME events associated with large flares.

Halo CMEs	AR location	Speed (km s^{-1})	Flares	D_{st} (nT)	IP structure	B_z (nT)	L_{neu}(Mm)	$|\theta|$ (deg)
1997/11/04, 06:10UT	S19W28	785	X2.1 at 05:58 UT	−110 on 11/07	Sheath	−12.53	36.30	90.48
1998/04/29, 16:58UT	S17E22	1374	M6.8 at 16:37 UT	−85 on 05/02	...	−12.71	31.94	86.13
1998/05/01, 23:40UT	S18W09	585	M1.2 at 22:54 UT	−119 on 05/05	Sheath	−9.76	25.41	135.16
1998/05/02, 14:06UT	S17W15	938	X1.1 at 13:42 UT	−205 on 05/04	Sheath	−22.92	31.94	46.81
1998/11/05, 20:44UT	N22W18	1118	M8.4 at 19:55 UT	−149 on 11/08	MC-ESW	−11.68	58.81	91.52
1998/11/27, 08:30UT	S24E09*	434	M1.6 at 07:43 UT	−22 on 12/02	...	−1.90	0.0	78.46
1999/05/03, 06:06UT	N15E32*	1584	M4.4 at 06:02 UT	−20 on 05/03	...	−1.06	12.34	90.01
1999/05/10, 05:50UT	N16E19*	920	M2.5 at 05:31 UT	−49 on 05/13	...	−9.99	16.70	20.94
1999/06/22, 18:54UT	N22E37	1133	M1.7 at 18:29 UT	1 on 06/24	...	−4.78	3.63	173.83
1999/06/26, 07:31UT	N23E02	364	M2.3 at 05:12 UT	−17 on 06/29	...	−2.20	15.97	102.20
1999/06/29, 18:54UT	S14E01*	438	M1.6 at 19:13 UT	−25 on 07/03	...	−5.07	18.15	102.89
1999/06/30, 11:54UT	S15W04*	406	M1.9 at 11:30 UT	−7 on 07/04	...	−1.03	22.51	21.38
1999/07/28, 09:06UT	S15E02	462	M2.3 at 08:14 UT	−39 on 07/31	...	−5.94	23.23	15.47
1999/10/14, 09:26UT	N11E32	1250	X1.8 at 09:00 UT	−47 on 10/16	...	−2.82	73.33	142.81
1999/12/22, 02:30UT	N20E24*	570	M1.8 at 02:16 UT	−8 on 12/25	...	−2.13	38.48	105.58
1999/12/22, 19:31UT	N20E14	605	M5.3 at 19:04 UT	−8 on 12/25	...	−2.13	24.68	99.53
2000/01/18, 17:54UT	S19E08*	739	M3.9 at 17:27 UT	−97 on 01/23	...	−15.86	13.07	152.69
2000/02/08, 09:30UT	N27E24	1079	M1.3 at 09:00 UT	−24 on 02/11	...	−3.29	25.41	71.21
2000/02/12, 04:31UT	N26W23	1107	M1.7 at 04:10 UT	−67 on 02/14	...	−6.71	13.07	83.14
2000/02/17, 21:30UT	S22W19	728	M2.5 at 18:52 UT	−26 on 02/21	...	−5.08	15.97	42.61

TABLE I
(Continued)

Halo CMEs	AR location	Speed (km s^{-1})	Flares	D_{st} (nT)	IP structure	B_z (nT)	L_{neu}(Mm)	$|\theta|$ (deg)
2000/06/06, 15:54 UT	N20E18	1119	X2.3 at 15:25 UT	−90 on 06/08	...	−7.25	41.38	78.22
2000/06/07, 16:30 UT	N23E03	842	X1.2 at 15:53 UT	−52 on 06/10	...	−5.33	34.12	73.98
2000/06/10, 17:08 UT	N22W38	1108	M5.2 at 17:02 UT	−37 on 06/13	...	−4.91	9.44	115.03
2000/07/11, 13:27 UT	N18E27*	1078	X1.0 at 13:10 UT	−43 on 07/13	...	−2.10	79.13	8.52
2000/07/14, 10:54 UT	N17W01	1674	X5.7 at 10:24 UT	−301 on 07/16	MC-SEN	−42.82	41.38	17.31
2000/07/25, 03:30 UT	N06W05*	528	M8.0 at 02:49 UT	−71 on 07/29	...	−11.88	23.96	58.38
2000/09/12, 11:54 UT	S17W09*	1550	M1.0 at 12:13 UT	−41 on 09/13	...	−7.55	0.0	113.57
2000/09/16, 05:18 UT	N13W02	1215	M5.9 at 04:26 UT	−201 on 09/17	Sheath	−21.28	14.52	52.68
2000/11/24, 05:30 UT	N20W05	994	X2.0 at 05:02 UT	−80 on 11/27	...	−10.78	43.56	41.29
2000/11/24, 15:30 UT	N21W10	1245	X2.3 at 15:13 UT	−80 on 11/27	...	−10.78	53.72	6.04
2000/11/24, 22:06 UT	N19W15	1005	X1.8 at 21:59 UT	−80 on 11/27	...	−10.78	20.33	31.61
2000/11/25, 09:30 UT	N19W21	675	M3.5 at 09:20 UT	−119 on 11/29	MC-WSE	−11.67	53.00	39.46
2000/11/25, 19:31 UT	N18W25	671	X1.9 at 18:44 UT	−119 on 11/29	MC-WSE	−11.67	37.03	38.88
2000/11/26, 17:06 UT	N19W31	980	X4.0 at 16:48 UT	−119 on 11/29	MC-WSE	−11.67	16.70	25.34
2001/01/20, 19:31 UT	S07E40	839	M7.7 at 21:20 UT	−52 on 01/24	...	−6.77	26.86	42.12
2001/03/24, 20:50 UT	N15E22*	906	M1.7 at 19:55 UT	−56 on 03/28	...	−6.75	0.0	64.38
2001/03/28, 01:27 UT	N16E08	427	M1.1 at 01:58 UT	−387 on 03/31	MC-SEN	−44.17	133.58	88.65
2001/03/28, 12:50 UT	N17E02	519	M4.3 at 12:40 UT	−387 on 03/31	MC-SEN	−44.17	138.66	70.79
2001/03/29, 10:26 UT	N16W12	942	X1.7 at 10:15 UT	−387 on 03/31	MC-SEN	−44.17	131.41	7.16
2001/04/06, 19:30 UT	S21E31	1270	X5.6 at 19:21 UT	−63 on 04/09	...	−4.43	51.55	60.30
2001/04/09, 15:54 UT	S21W04	1192	M7.9 at 15:34 UT	−271 on 04/11	Sheath	−17.62	58.08	82.10

(Continued on next page)

TABLE I
(Continued)

Halo CMEs	AR location	Speed (km s⁻¹)	Flares	D_{st} (nT)	IP structure	B_z (nT)	L_{neu} (Mm)	$|\theta|$ (deg)
2001/04/10, 05:30 UT	S23W09	2411	X2.3 at 05:26 UT	−271 on 04/09	Sheath	−17.62	42.83	81.59
2001/04/11, 13:31 UT	S22W27	1103	M2.3 at 13:26 UT	−77 on 04/13	…	−3.698	22.51	87.12
2001/04/26, 12:30 UT	N20W12	1006	M7.8 at 13:12 UT	−47 on 04/29	…	−13.38	41.38	41.79
2001/08/25, 16:50 UT	S17E34	1433	X5.3 at 16:45 UT	−23 on 08/28	…	−4.36	53.00	22.59
2001/09/24, 10:30 UT	S16E23	2402	X2.6 at 10:38 UT	−102 on 09/26	DG^a	−10.30	38.48	62.13
2001/09/28, 08:54 UT	N13E18*	1000	M3.3 at 08:30 UT	−148 on 10/01	MC-NES	−12.88	15.25	51.66
2001/10/09, 11:30 UT	S28E08*	973	M1.4 at 11:13 UT	−71 on 10/12	…	−7.11	0.0	116.29
2001/10/19, 01:27 UT	N16W18	558	X1.6 at 01:05 UT	−187 on 10/21	Sheath	−16.93	36.30	118.07
2001/10/19, 16:50 UT	N15W29	901	X1.6 at 16:30 UT	−187 on 10/21	Sheath	−16.93	31.22	122.39
2001/10/25, 15:26 UT	S16W21	1092	X1.3 at 15:02 UT	−157 on 10/28	MC-NES	−10.70	42.83	62.98
2001/11/04, 16:35 UT	N06W18	1810	X1.0 at 16:20 UT	−292 on 11/06	MC-ESW	−68.10	25.41	50.73
2001/11/28, 17:30 UT	N05E17	500	M6.9 at 16:35 UT	−3 on 12/02	…	−0.71	51.55	76.64
2002/03/15, 23:06 UT	S09W02	957	M2.2 at 23:10 UT	−37 on 03/19	…	−10.10	18.88	30.62
2002/04/15, 03:50 UT	S15W01*	720	M1.2 at 03:55 UT	−127 on 04/18	MC-SWN	−12.24	42.11	21.35
2002/04/17, 08:26 UT	S16W28	1240	M2.6 at 08:24 UT	−149 on 04/20	Sheath	−13.40	47.92	30.97
2002/07/15, 20:30 UT	N19W01	1151	X3.0 at 20:08 UT	−17 on 07/18	…	−3.84	60.26	91.06
2002/07/18, 08:06 UT	N20W25*	1099	X1.8 at 07:44 UT	−34 on 07/20	…	−4.49	52.27	91.47
2002/07/26, 22:06 UT	S19E22	818	M8.7 at 21:12 UT	−14 on 07/28	…	−2.73	87.85	158.02
2002/08/16, 12:30 UT	S14E20	1585	M5.2 at 12:32 UT	−38 on 08/17	…	−3.39	103.82	57.50
2002/12/19, 22:06 UT	N17W09*	1092	M2.7 at 21:53 UT	−48 on 12/21	…	−1.78	3.63	98.46
2003/05/27, 06:50 UT	S07W12	509	M1.6 at 06:26 UT	−73 on 05/30	…	0.82	63.34	142.38

(Continued on next page)

TABLE I
(Continued)

Halo CMEs	AR location	Speed (km s^{-1})	Flares	D_{st} (nT)	IP structure	B_z (nT)	L_{neu} (Mm)	$|\theta|$ (deg)
2003/05/27, 23:50 UT	S07W17	964	X1.3 at 23:07 UT	−131 on 05/30	Sheath	−15.00	56.63	141.31
2003/05/29, 01:27 UT	S07W33	1237	X1.2 at 01:05 UT	−131 on 05/30	Sheath	−15.00	79.86	157.35
2003/10/28, 11:30 UT	S16E08	2459	X17.2 at 11:10 UT	−363 on 10/30	MC-WSE	−24.49	206.18	171.15
2003/10/29, 20:54 UT	S15W02*	2029	X10.0 at 20:49 UT	−401 on 10/30	Sheath	−29.18	145.93	76.32
2004/04/06, 13:01 UT	S18E15*	1368	M2.4 at 13:28 UT	−31 on 04/07	…	−1.22	0.0	63.71
2004/07/23, 16:06 UT	N04W08	824	M2.2 at 17:28 UT	−197 on 07/27	MC-NES	−15.29	71.87	6.69
2004/07/25, 14:54 UT	N04E30	1333	M2.2 at 13:49 UT	−197 on 07/27	MC-NES	−15.29	79.13	23.15
2004/09/14, 10:12 UT	N09W18	462	M1.5 at 09:30 UT	−43 on 09/15	…	−8.90	15.25	87.41
2004/11/03, 16:06 UT	N07E38	1068	M5.0 at 15:47 UT	−10 on 11/04	…	−2.47	26.14	159.06
2004/11/06, 01:31 UT	N08E05	818	M9.3 at 00:34 UT	−373 on 11/08	MC-SEN	−43.80	74.05	39.64
2004/11/07, 16:54 UT	N08W16	1759	X2.0 at 16:06 UT	−373 on 11/08	MC-SEN	−43.83	66.07	36.11

TABLE II

Comparison of magnetic gradient thresholds in source regions identification.

Threshold (G Mm^{-1})	M-flare identification			X-flare identification			Overall (%)
	Correct	Wrong	Percentage (%)	Correct	Wrong	Percentage (%)	
25	25	20	55.6	24	4	85.7	67.1
50	30	15	66.7	25	3	89.3	75.3
75	29	16	64.4	25	3	89.3	74.0
100	28	17	62.2	26	2	92.9	74.0
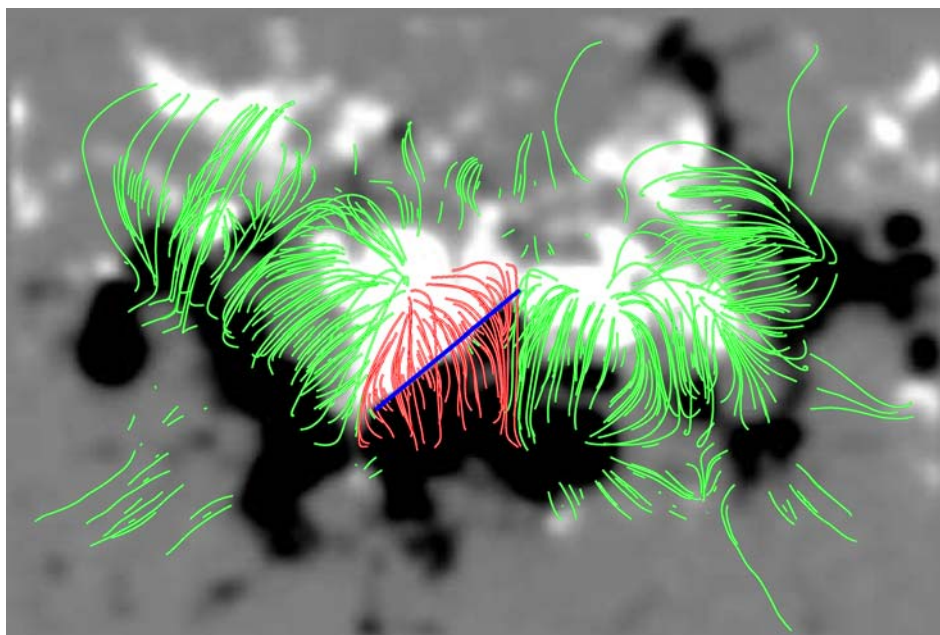
Figure 2. Background is an MDI magnetogram taken at 09:36 UT on July 14, 2000. *Over-plotted* are potential field lines. The segment of a *thick blue line* indicates the position of the main magnetic neutral line. The field lines that cross the main neutral line are displayed with *red color*.

or some additional constraints and thus are less suitable, in their present state, for automated processes.

Let us illustrate how magnetic orientation of a CME can be quantified by using the well studied July 14, 2000, eruption. A halo CME on July 14, 2000, first appeared in the LASCO/C2 FOV at 10:54 UT. Simultaneously, a great X5.7 solar flare was observed near the disk center in active region NOAA 9077. The SOHO MDI full disk magnetogram taken at 09:36 UT on July 14, 2000, is shown in Figure 1a. The extrapolated potential field is presented in Figure 2. The magnetic field lines are plotted in either red or green color, depending on whether their projection is intersect with the HGNL (Figure 1c).

Figure 3 illustrates how the magnetic orientation angle θ is defined and calculated for a source region identified by the HGNL method. An extrapolated field line, L, is shown by red color, while the gradient neutral line (N) is plotted in blue. Two arbitrary points on the field line L are indicated with letters P and A. Projection of P and A on the horizontal plane (photosphere) are P$'$ and A$'$, correspondingly. Hence, the line P$'$A$'$ is the projection of L on the surface and it intersects with the gradient neutral line N. The angle between P$'$A$'$ and the southward direction is defined as the orientation angle θ. In the entire active region, numerous field lines have projections that intersect the HGNL and each of them has its unique
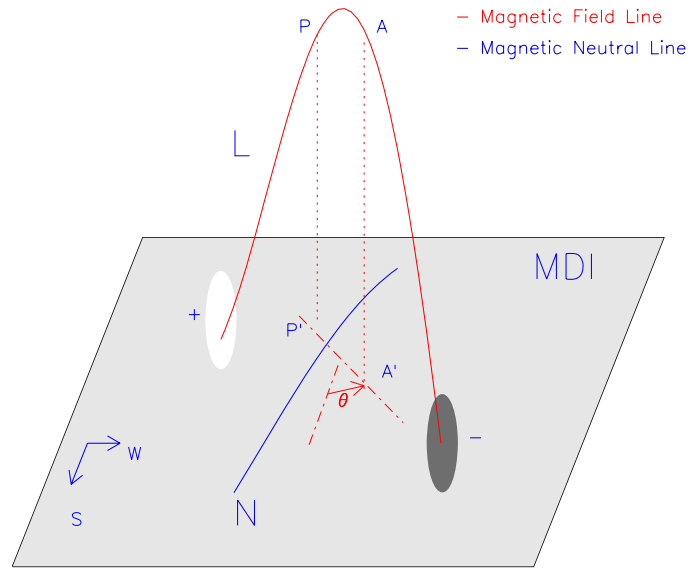
Figure 3. Definition of the magnetic orientation angle θ. *Blue line* N represents the main neutral line. P′A′ is projection of the field line L on the plane. Angle between P′A′ and the direction toward south pole is the orientation angle for this particular field line.

orientation angle. Thus, the average orientation angle determined for the entire active region is calculated as the median of individual θ_i. In order to get an accurate orientation angle θ, for each event we extrapolated over several thousands of field lines. The number of intersected field lines to calculate the average angle are always more than hundreds. The overall orientation angle of this particular event is about $11.65°$, indicating southward magnetic field component associated with the neutral line.

3.3. THE EFFECT OF ICMES

ICME is the manifestation of a CME in interplanetary (IP) space. Depending on the magnetic orientation, an ICME may or may not trigger a large geomagnetic storm. There are two magnetic structures in an ICME that can carry intense southward IMFs (Gonzalez, Tsurutani, and Clúa de Gonzalez, 1999): the sheath region behind the forward shock (Tsurutani *et al.*, 1988; Tsurutani and Gonzalez, 1997) and an ICME body that can be often observed as a MC (Klein and Burlaga, 1982). In the sheath region solar wind plasma is heated, compressed and piled up in front of the ICME body. Magnetic fields with a rapidly fluctuating orientations are characteristic for the sheath region. A MC is a large-scale and organized structure that can possess long intervals of the southwardly directed fields, therefore it is expected to be more geoeffective than sheath region (Zhang *et al.*, 2004).

Generally, MCs could be modelled by a flux rope model (Mulligan and Russell, 2002). The internal magnetic field configuration within a MC is cylindrically symmetric and force-free, with constant α, where α is the magnitude of the magnetic helicity (Goldstein, 1983; Burlaga, 1998). According to this model, Bothmer and Schwenn (1998) described four types of MC structures: SWN, NES, SEN, and NWS. In the GSE coordinate system, these types of MCs will produce different magnetic signatures in the spacecraft measurements. Assuming that the axis of a MC lies in the ecliptic plane, the SEN-type clouds are those whose magnetic field vector turns from south (S, negative B_z) at the leading edge to east (E, positive B_y) at the cloud's axis and finally to the north (N, positive B_z) at its trailing edge. Such a cloud is left handed (negative helicity). A SWN-type cloud has its axial field pointed westward, while the azimuthal field rotates from S to N direction. This cloud is right handed (positive helicity). Similarly, one can deduct the magnetic field rotation in NES- and NWS-type clouds. Mulligan and Russell (1998) introduced another four types of MCs: ESW, ENW, WSE, and WNE. The axes of these MC structures are perpendicular to the ecliptic plane. Those MCs with an axes that lies approximately in the ecliptic plane are called bipolar clouds because B_z can change its sign (rotate) during the passage of satellite. Unipolar clouds have their axes nearly normal to the ecliptic plane and thus B_z component, measured by a satellite, is of the same sign.

By studying 34 ICME events, Wu and Lepping (2002) found that geomagnetic storms can be produced either by a sheath region, the leading or trailing field of a MC or both the sheath field and the MC itself. In their study, when only bipolar MCs were considered a cloud's leading field is found to be the major driving force for storms (44.1%). Zhang *et al.* (2004) examined the relationship between 271 storms and 104 magnetic clouds. It is found that the leading field is the most geoeffective region and 72% of intense storms were caused by MCs. Huttunen *et al.* (2005) examined 73 MCs observed by the WIND and ACE instruments in solar cycle 23 and found that in 16 cases the storm was caused by sheath region preceding the MC and for 21 events neither the sheath nor the MC triggered the storm.

To determine the effect of magnetic topology of the CME source region on the B_z of IMF and the D_{st} index, we need to understand ICME's IP structures and distinguish between magnetic fields of the sheath region and an ICME body, and identify a storm driver. Table I, column 6, lists drivers of geomagnetic storms with $D_{st} \leq -100$ nT. They are identified based on either data from OMNI database[3] or obtained from several other studies (Wang, Ye, and Wang, 2003; Wang *et al.*, 2005; Zhang *et al.*, 2004; Xue *et al.*, 2005; Huttunen *et al.*, 2005). Our criteria to identify MC are as follows: (1) Smooth field rotation is required for all cases in this study. (2) Enhanced field is qualitatively compared with the ambient solar wind values. The reference field enhancement tended to be $\geq 50\%$ with some exception; (3) the
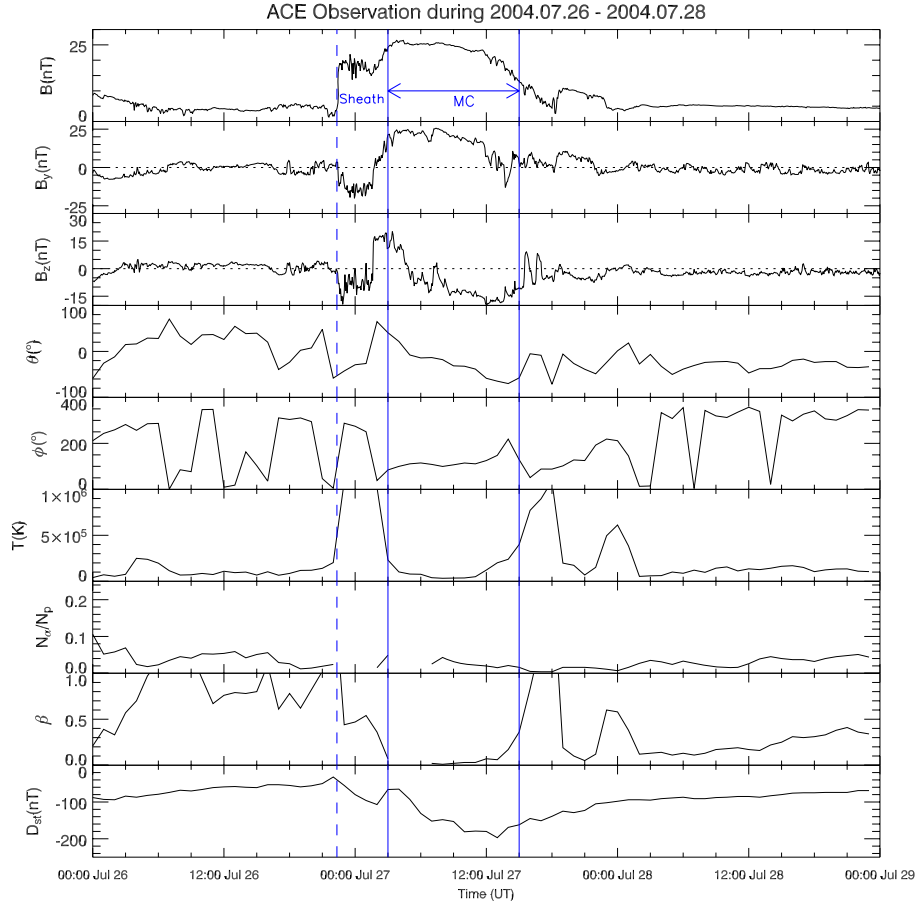
[3]http://cdaweb.gsfc.nasa.gov/.

Figure 4. ACE measurements of IMF from July 26 to 28, 2004 (in GSE). From *top* to *bottom* are magnetic field strength (*B*), *y*- and *z*-components of magnetic fields (*B_y*, *B_z*), the latitude (*θ*) and longitude (*φ*) angles, proton temperature (*T*), density ratio (N_α/N_p), plasma pressure (*β*), and the D_{st} index.

ratio of N_α/N_p is $\geq$0.08–0.10 (Lynch *et al.*, 2003; Xue *et al.*, 2005); (4) and the average values of plasma pressure *β* is $\leq$0.5 (Huttunen *et al.*, 2005).

Figures 4 and 5 show ACE measurements data and D_{st} index for two MCs in observed in 2004. Panels from top to bottom are the total interplanetary magnetic field *B*, east–west B_y and north–south B_z components of IMF (GSE system), latitude (*θ*) and longitude (*φ*) of the solar wind magnetic field in RTN coordinates, proton temperature *T*, ratio of N_α/N_p, magnetic plasma pressure *β*, and D_{st} index. The boundaries of each MCs are indicated with vertical solid lines and the dashed lines indicate the beginning of sheath regions. All data are one-hour averages except the magnetic field data, which are four-minute averages.
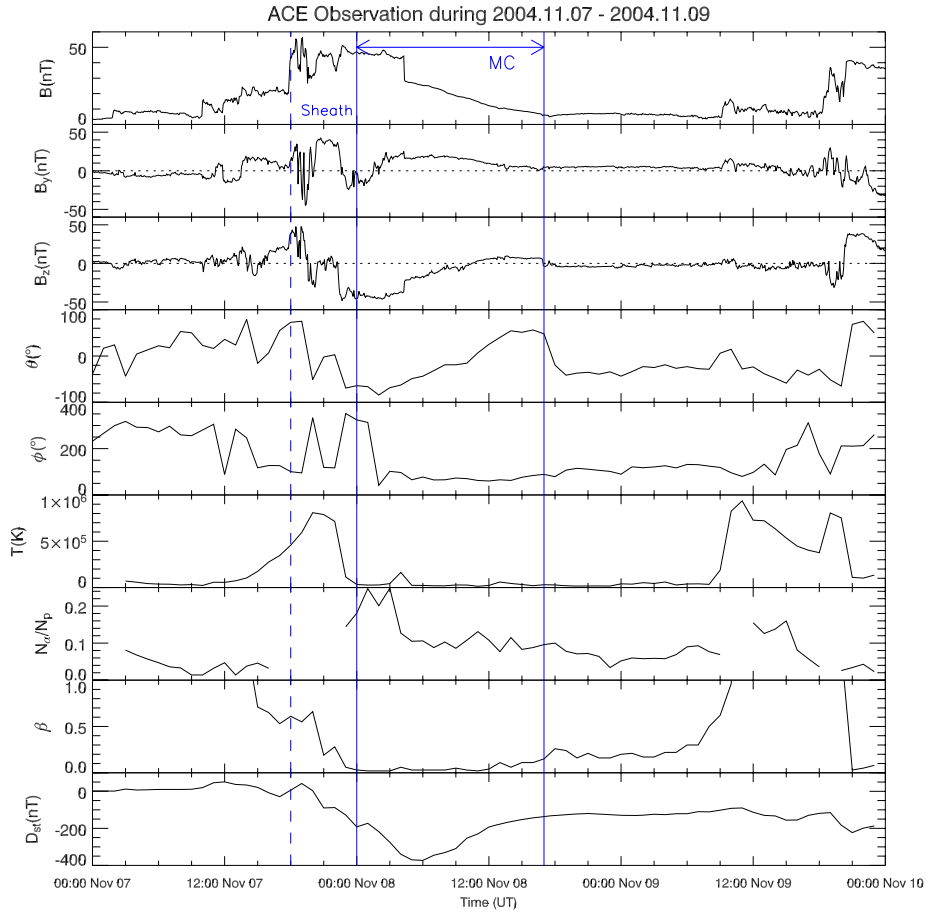
Figure 5. ACE measurements of IMF from November 7 to 9, 2004 (in GSE). From *top* to *bottom* are magnetic field strength (B), y- and z-components of magnetic fields (B_y, B_z), the latitude (θ) and longitude (ϕ) angles, proton temperature (T), density ratio (N_α/N_p), plasma pressure (β), and the D_{st} index.

In these two events, the D_{st} index peaked at 14:00 UT on July 27 (-197 nT) and at 07:00 UT on November 8 (-373 nT). The cause of these two geomagnetic storms was the intense southward IMF in the corresponding MCs. Figure 4 shows that southward IMF in the July 27 MC lasted for about 12 h and it attained the maximum value of -17.7 nT. In this event, the field vector rotated from the northern direction (N) at the leading edge to the southern (S) at the trailing edge and it was eastwardly directed at the cloud's axis (E, positive B_y). Such a MC is of the NES type and it was the trailing field (TF) that caused the geomagnetic storm ($D_{st} = -197$ nT). Figure 5 shows a super geomagnetic storm ($D_{st} = -373$ nT) caused by another bipolar MC. The maximum southward B_z was -46.17 nT, nearly three times stronger than that in Figure 4. The B_z duration was about 17 h. The magnetic field vector in this SEN

MC changed from south (S) at the leading, to east (E) at the axis, to north (N) at the trailing edge. Thus, the geomagnetic storm was a result of the strong southward leading field.

4. Results

In Table I we list results of our study for total of 73 halo CMEs. The first column shows the date and time of the halo CMEs, the second column provides locations of the source regions determined from the magnetic gradient method. The next columns are the linear speed of a CME in the plane of the sky (POS), magnitude and time of associated solar flares, the corresponding D_{st} index, the IP structures of ICME that caused the storm (only for strong storms), the maximum southward component B_z, the length of main NL and the orientation of magnetic structure in the source region.

4.1. Effectiveness of HGNL method on identification of flaring active regions

Figure 6 shows the distribution of the number of events versus their calculated L_{neu}. For comparison, the events associated with X-class or M-class flares are separated and displayed in panels (a) and (b). The median L_{neu} in panel (a) was in the range of 30–60 Mm, while it was much longer than that found in M-class events. Meanwhile, the range of L_{neu} shown in panel (a) (up to 200 Mm) is also wider than that in panel (b). This is probably because that X flares are extreme events and their tendency to occur at the location with high concentration of free magnetic energy is much higher than that for the M-class flares.

In 25% of cases (18 out of 73, indicated by asterisks) the magnetic gradient method produced wrong results and thus the location of source regions was different from that listed in NOAA SEC reports. Furthermore, 11 out of these 18 events (61%) have L_{neu} shorter than 20 Mm. Table II shows how the selection of the gradient threshold affects the source identification. A sufficiently high threshold may improve the accuracy of identification from 67 up to 75%. There is a limit on the gradient threshold, i.e., we can only improve accuracy to a certain extent: further increase of the threshold value does not lead to a significant increase in the accuracy. In this study, the highest overall accuracy is about 75% when the threshold was $50\,\mathrm{G\,Mm^{-1}}$. When we divided events based on the magnitudes of associated flares, the HGNL method produced better results for X-class flares (89% success) as compared to the M-class flares (68% success).

The limitation of HGNL method could be due to the fact that several active regions are in the same full-disk MDI magnetogram. The region identified by HGNL method is indeed 'active', however, it was not responsible for any CME eruptions.
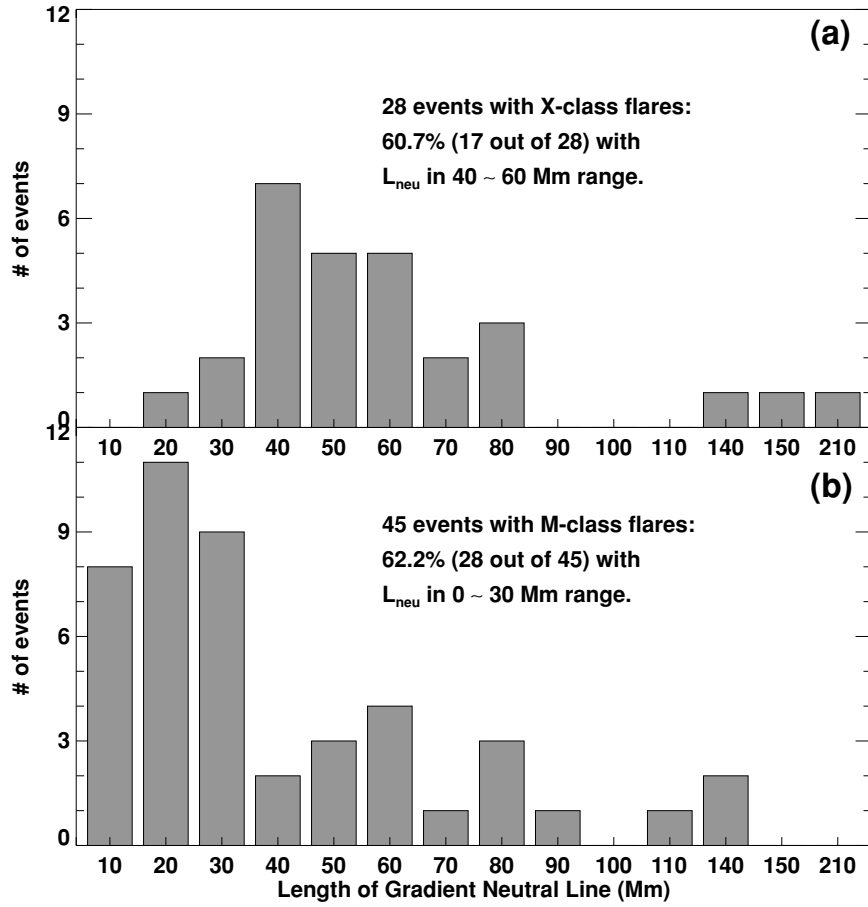
Figure 6. Distribution of the calculated length of magnetic gradient neutral line of 73 CME events. The width of the bar is 10 Mm.

Such a limit might be solved by the combination of LASCO information about CMEs, or the power spectra method proposed by Abramenko (2005). Therefore, we conclude that the prediction on the CME source region with the HGNL method is feasible, especially for those events associated with X-class flares.

4.2. RELATIONSHIP BETWEEN SURFACE MAGNETIC ORIENTATION θ, IMF B_z, AND THE D_{st} INDEX

In Figure 7, we plot the magnetic orientation angle θ versus the D_{st} index. Blue triangles represent super geomagnetic storms ($D_{st} \leq -200\,\mathrm{nT}$), green crosses are intense storms ($-200\,\mathrm{nT} \leq D_{st} \leq -100\,\mathrm{nT}$), while red diamonds are moderate storms ($D_{st} \geq -100\,\mathrm{nT}$). Labels next to data points indicate the type of the IP structure
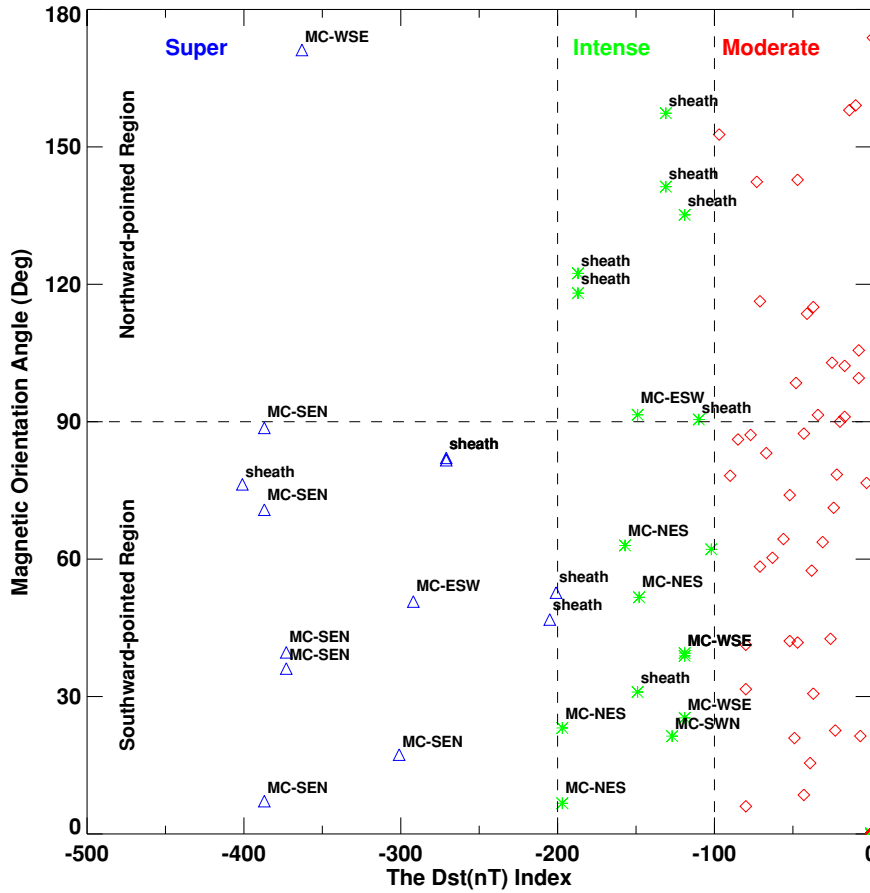
Figure 7. Magnetic orientation angle, θ, versus the D_{st} index. The *blue triangles* represent super storms, *green stars* show intense storms, and *red diamonds* are moderate storms. The *label* indicates the responsible interplanetary magnetic structure for the storm.

that caused the storm (see Table I). Those events with northward magnetic orientation ($|\theta| \geq 90°$) appear in the upper half of the graph, while southwardly directed events are in the lower part. The moderate storms for which we had difficulties in MC identification are not included in the figure.

The graph shows that about 92% of super geomagnetic storms (12 out of 13) had their orientation angle $|\theta| < 90°$, thus indicating the southward orientation of the associated solar source regions. For the intense and moderate storms, the southward orientation was found in 59% (10 out of 17) and 63% (27 out of 43) of cases, respectively. Table III summarizes the results and illustrates that largest geomagnetic storms are more likely to be associated with the orientation angle smaller than 90°. We would like to emphasize that the orientation angle obtained from solar surface data should not be considered as a prediction of the orientation of

TABLE III

Magnetic orientation of solar source regions and geomagnetic storms.

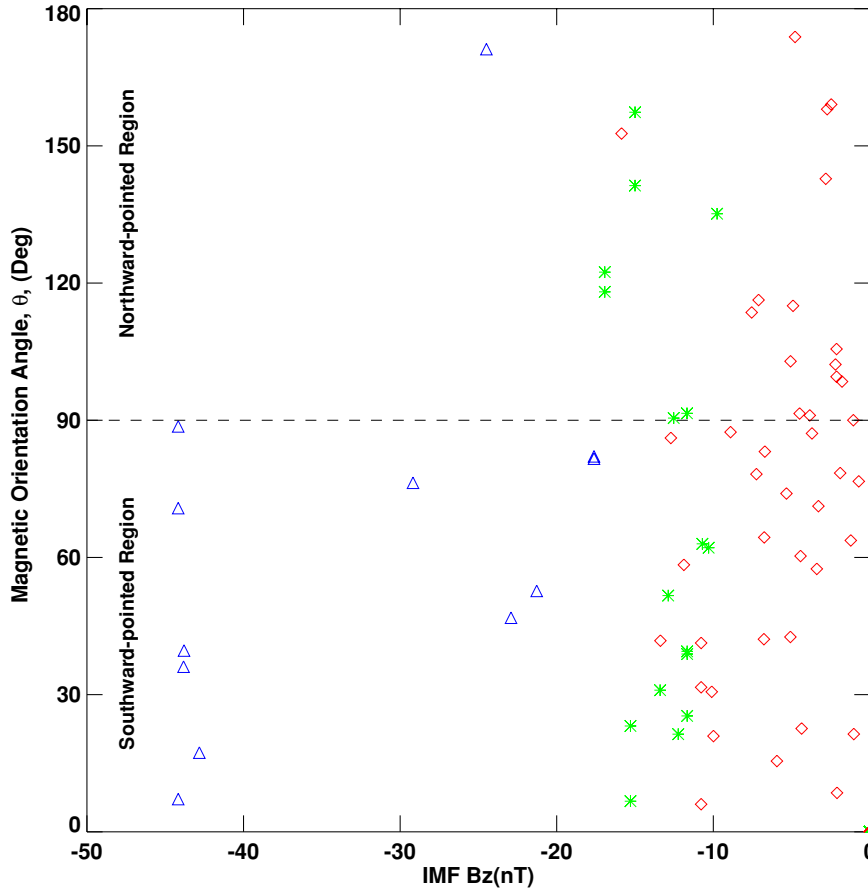| D_{st} (nT)	$\|\theta\| < 90°$(S)	$\|\theta\| \geq 90°$ (N)	Total	Fraction of $\theta < 90°$ (%)
$D_{st} \leq -200$	12	1	13	92
$D_{st} \leq -150$	15	3	18	83
$D_{st} \leq -100$	22	8	30	73

Figure 8. The magnetic orientation angle θ versus corresponding IMF B_z. In the case of super geomagnetic storms produced by strong negative B_z, the corresponding source regions also had southward-oriented magnetic fields.

a MC at 1 AU. Instead, it is a parameter that indicates, when $\|\theta\| < 90°$, whether the azimuthal field in an ICME is expected to have southwardly directed component.

We found that totally there are eight super and intense storms (one super, seven intense) whose source regions on the solar surface were associated with

northward-oriented angles. Their IP structures shown that six of them were caused by the southward B_z in the sheath region. The orientation angles for the two exceptions on November 5, 1998, and October 28, 2003, were 91.52 and 171.15, respectively. The IP structure of the first event (intense storm, $D_{st} = -149$ nT) is identified as ESW. Many studies from different perspectives were made on the second case because of its large D_{st} index (super storm, $D_{st} = -363$ nT) and high intensity of X17.2 flare (Yang *et al.*, 2004; Metcalf, Leka, and Mickey, 2005; Yurchyshyn, Hu, and Abramenko, 2005). Yurchyshyn, Hu, and Abramenko (2005) concluded that this magnetic storm was caused by a MC of WSE type. Both storms were almost entirely due to the strong axial field, which led to the reconnection and then the storm. Gopalswamy *et al.* (2005) obtained the same conclusion that the unipolar MC is geoeffective when the axial field vector directs southward, after the study of a super geomagnetic storm ($D_{st} = -472$ nT) occurred on November 20, 2003. Therefore, the topology of the source region, at least of those super storms, plays a key role in determining the magnetic structure of an interplanetary ejecta, and furthermore the occurrence of geomagnetic storms.

Figure 8 shows a similar graph as in Figure 7 but the D_{st} index was replaced by IMF B_z. The trend is similar: for super and intense geomagnetic storms the orientation angle tends to be smaller than $90°$, i.e., the corresponding source regions have southward orientation.

5. Conclusions and Discussion

Automatic prediction of super geomagnetic storms ($D_{st} \leq -200$ nT) is an important task in space weather programs. In this paper, the automatic prediction is performed in the following procedures:

– Identification of CME source regions: Longitudinal magnetic gradient and gradient neutral lines are calculated from full-disk SOHO MDI magnetograms by using a suitable threshold value (50 G Mm^{-1}). The solar active regions most probable to launch a CME are located on the solar disk by identifying locations with the largest length of the strongest HGNL. Due to the projection effect on HGNL calculation, those active regions close to the limb of solar disk might not be identified by HGNL method.

– Potential field extrapolation: A potential field model is used to extrapolate coronal magnetic fields of the selected source region. Those extrapolated field lines that intersect with the strongest HGNL are chosen to calculate the magnetic orientation angle θ.

– Prediction: The magnetic orientation angle is used to predict the presence of southward B_z in an ejecta: The events associated with $| \theta | < 90°$ are more likely to cause a super geomagnetic storm.

Based on a study of 73 halo CMEs associated with M-class and X-class flares that occurred between 1996 and 2004, we have reached the following conclusions:

1. Magnetic gradient method is proved to be a viable approach to locate the source region of either CMEs or flares. The overall accuracy is about 75% (55 out of 73 events). It appears to be more accurate in identification of sources of X-class flares (89%) than M-class flares (68%).
2. The magnetic orientation angle θ, determined from a potential field model, can be used to predict the probability of super geomagnetic storms ($D_{st} \leq -200\,$nT). About 92% of the super storms (12 out of 13 events) were associated with solar source regions that had orientation angles $|\,\theta\,|$ smaller than 90°, i.e., southward-oriented magnetic fields. Geomagnetic storms with northward-oriented source region ($|\,\theta\,| \geq 90°$) may be caused by the sheath region and/or unipolar magnetic clouds.
3. The relationship between the D_{st} index and the orientation angle indicates that, at least for super storms, the topology of the source region plays a key role in determining the magnetic structure of an interplanetary ejecta.

Acknowledgements

References

Abramenko, V.I.: 1986, *Glav. Astr. Obs.* **8**, 83.
Abramenko, V.I.: 2005, *Astrophys. J.* **629**, 1141.
Bothmer, V. and Schwenn, R.: 1994, *Space Sci. Rev.* **95**, 147.
Bothmer, V. and Schwenn, R.: 1995, *J. Geomag. Geoelectr.* **47**, 1127.
Bothmer, V. and Schwenn, R.: 1998, *Ann. Geophys.* **16**, 1.
Brueckner, G.E. *et al.*: 1998, *Geophys. Res. Lett.* **25**, 3019.
Burlaga, L.F., Sittler, E., Mariani, F., and Schwenn, R.: 1981, *J. Geophys. Res.* **86**, 6673.
Burlaga, L.F. *et al.*: 1998, *J. Geophys. Res.* **103**, 277.
Cane, H.V., Richardson, I.G., and St. Cyr, O.C.: 2000, *Geophys. Res. Lett.* **27**, 3591.
Deng, Y., Wang, J., Yan, Y., and Zhang, J.: 2001, *Solar Phys.* **204**, 11.
Dungey, J.W.: 1961, *Phys. Res. Lett.* **6**, 47.
Falconer, D.A.: 2001, *J. Geophys. Res.* **106**, 25185.
Falconer, D.A., Moore, R.L., and Gary, G.A.: 2003, *J. Geophys. Res.* **108**, SSH11.
Fletcher, L. and Hudson, H.S.: 2001, *Solar Phys.* **204**, 69.

Gallagher, P.T., Moon, Y.J., and Wang, H.: 2002, *Solar Phys.* **209**, 171.

Goldstein, H.: 1983, in M. Neugebauer (ed.), *Solar Wind Five*, *NASA CP-2280*, p. 731.

Gonzalez, W.D. *et al.*: 1994, *J. Geophys. Res.* **99**, 5771.

Gonzalez, W.D., Tsurutani, B.T., and Clúa de Gonzalez, A.L.: 1999, *Space Sci. Rev.* **88**, 529.

Gopalswamy, N. *et al.*: 2000, *Geophys. Res. Lett.* **27**, 145.

Gopalswamy, N. *et al.*: 2005, *Geophys. Res. Lett.* **32**, L12S09.

Hagyard, M.J.: 1990, *Memor. Soc. Astron. Ital.* **61**, 337.

Howard, R.A., Michels, D.J., Sheeley, N.R., Jr., and Koomen, M.J.: 1982, *Astrophys. J.* **263**, L101.

Howard, T.A. and Tappin, S.J.: 2005, *Astron. Astrophys.* **440**, 373.

Hudson, H.S., Lemen, J.R., St. Cyr, O.C., Sterling, A.C., and Webb, D.F.: 1998, *Geophys. Res. Lett.* **25**, 2481.

Huttunen, K.E.J., Schwenn, R., Bothmer, V., and Koskinen, H.E.J.: 2005, *Ann. Geophys.* **23**, 625.

Klein, L.W. and Burlaga, L.F.: 1982, *J. Geophys. Res.* **87**, 613.

Kosovichev, A.G. and Zharkova, V.V.: 2001, *Astrophys. J.* **550**, L105.

LaBonte, B.J., Mickey, D.L., and Leka, K.D.: 1999, *Solar Phys.* **189**, 1.

Liu, C., Deng, N., Liu, Y., Falconer, D., Goode, P.R., Denker, C., and Wang, H.: 2005, *Astrophys. J.*, in press.

Liu, Y. and Zhang, H.: 2001, *Astron. Astrophys.* **372**, 1019.

Lynch, B.J. *et al.*: 2003, *J. Geophys. Res.* **108**, 1239.

Marubashi, K.: 1997, in N. Crooker, J.A. Joselyn, and J. Feynman (eds.), *Coronal Mass Ejections*, *Geophys. Monograph*, Vol. 99, American Geophysical Union, p. 147.

MacQueen, R.M. and Fisher, R.R.: 1983, *Solar Phys.* **89**, 89.

Masuda, S., Kosugi, T., and Hudson, H.S.: 2001, *Solar Phys.* **204**, 55.

McAllister, A.H. and Martin, S.F.: 2000, *Adv. Space Res.* **26**, 469.

Metcalf, T.R., Leka, K.D., and Mickey, D.L.: 2005, *Astrophys. J.* **623**, L53.

Mickey, D.L., Canfield, R.C., Labonte, B.J., Leka, K.D., Waterson, M.F., and Weber, H.M.: 1996, *Solar Phys.* **168**, 229.

Moon, Y.-J., Wang, H., Spirock, T.J., Goode, P.R., and Park, Y.D.: 2003, *Solar Phys.* **217**, 79.

Mulligan, T. and Russell, C.T.: 1998, *Geophys. Res. Lett.* **25**, 2959.

Mulligan, T. and Russell, C.T.: 2002, *J. Geophys. Res.* **106**, A6, 10581.

Park, Y.D., Moon, Y.-J., Kim, I.S., and Yun, H.S.: 2002, *Astrophys. Space Sci.* **279**, 343.

Prasad, C.B.: 2000, *Astrophys. Space Sci.* **274**, 463.

Rust, D.M.: 1994, *Geophys. Res. Lett.* **21**, 241.

Sheeley, N.R., Jr., Howard, R.A., Koomen, M.J., and Michels, D.J.: 1983, *Astrophys. J.* **272**, 349.

St. Cyr, O.C. *et al.*: 2000, *J. Geophys. Res.* **105**, 18169.

Sterling, A.C. and Hudson, H.S.: 1997, *Astrophys. J.* **491**, L55.

Tanagra, K.: 1991, *Solar Phys.* **136**, 133.

Tang, F.: 1983, *Solar Phys.* **89**, 43.

Thompson, B.J. *et al.*: 1999, *Astrophys. J.* **517**, L151.

Tsurutani, B.T. and Gonzalez, W.D.: 1997, in W.D. Gonzalez, B.T. Tsurutani, and Y. Kamide (eds.), *Magnetic Storms*, *Geophysics Monograph*, Vol. 98, p. 77.

Tsurutani, B.T., Gonzalez, W.D., Tang, F., Akasofu, S.I., and Smith, E.J.: 1998, *J. Geophys. Res.* **93**, 8519.

Tsurutani, B.T.: 2001, in I.A. Daglis (ed.), *Space Storms and Space Weather Hazards*, Kluwer Academic Publishers, Dordrecht, p. 103.

Vennerstroem, S.: 2001, *J. Geophys. Res.* **106**, 29175.

Wang, H., Ewell, M.W., Zirin, H., and Ai, G.: 1994, *Astrophys. J.* **424**, 436.

Wang, H., Liu, C., Zhang, H., and Deng, Y.: 2004, *Astrophys. J.*, submitted for publication.

Wang, H., Song, H., Yurchyshyn, V., Deng, Y., Zhang, H., Falconer, D., and Li, J.: 2005, *Astrophys. J.*, submitted for publication.

Wang, Y.M., Ye, P.Z., Wang, S., Zhou, J.P., and Wang, J.: 2002, *J. Geophys. Res.* **107**, 2.

Wang, Y.M., Ye, P.Z., and Wang, S.: 2003, *J. Geophys. Res.* **108**, 1370.

Wang, Y.M., Ye, P.Z., Wang, S., Zhou, G.P., Wang, S.J., Wang, S., Yan, Y.H., and Wang, J.X.: 2005, *Solar Phys.* **226**, 337.

Warmuth, A. *et al.*: 2004, *Astron. Astrophys.* **418**, 1117.

Webb, D.F. *et al.*: 2000, *J. Geophys. Res.* **105**, 7491.

Wu, C-.C. and Lepping, R.P.: 2002, *J. Geophys. Res.* **107**, SMP19-1.

Wu, C-.C. and Lepping, R.P.: 2005, *J. Atmos. Solar Terr. Phys.* **67**, 283.

Xue, H. *et al.*: 2005, *Planet. Space Sci.* **53**, 443.

Yang, G., Xu, Y., Cao, W., Wang, H., Denker, C., and Rimmele, T.R.: 2004, *Astrophys. J.* **617**, L151.

Yashiro, S., Gopalswamy, N., Michalek, G., St. Cyr, O.C., Plunkett, S.P., Rich, N.B., and Howard, R.A.: 2004, *J. Geophys. Res.* **109**, A07105.

Yurchyshyn, V., Wang, H., Goode, P.R., and Deng, Y.: 2001, *Astrophys. J.* **563**, 381.

Yurchyshyn, V., Wang, H., and Abramenko, V.: 2004, *Space Weather* **2**(2).

Yurchyshyn, V., Hu, Q., and Abramenko, V.: 2005, *Space Weather* **3**(8).

Zhang, H.: 2001, *Astrophys. J.* **557**, L71.

Zhang, J. *et al.*: 2003, *Astrophys. J.* **582**, 520.

Zhang, J., Liemohn, M.W., Kozyra, J.U., Lynch, B.J., and Zurbuchen, T.H.: 2004, *J. Geophys. Res.* **109**, 09101.

Zhao, X.P. and Webb, D.F.: 2003, *J. Geophys. Res.* **108**, 4.